SUPPORTING INFORMATION

Iridium Oxide for the Oxygen Evolution Reaction: Correlation between Particle Size, Morphology and the Surface Hydroxo Layer from *Operando* XAS

Daniel F. Abbott[a,‡], Dmitry Lebedev[b,‡], Kay Waltar[a,◊], Mauro Povia[a], Maarten Nachtegaal[c], Emiliana Fabbri[a], Christophe Copéret[b], Thomas J. Schmidt[a,d]*

[a]*Electrochemistry Laboratory, Paul Scherrer Institut, CH−5232 Villigen PSI, Switzerland*
[b]*Department of Chemistry and Applied Biosciences, Vladimir Prelog Weg. 1-5, ETH Zürich, CH−8093 Zürich, Switzerland*
[c]*Paul Scherrer Institut, CH−5232 Villigen PSI, Switzerland*
[d]*Laboratory of Physical Chemistry, ETH Zürich, CH−8093 Zürich, Switzerland*
[◊]*Surface Physics Laboratory, Department of Physics, University of Zürich, Winterthurerstrasse 190, CH-8057 Zürich, Switzerland*

‡ *Equal contribution*

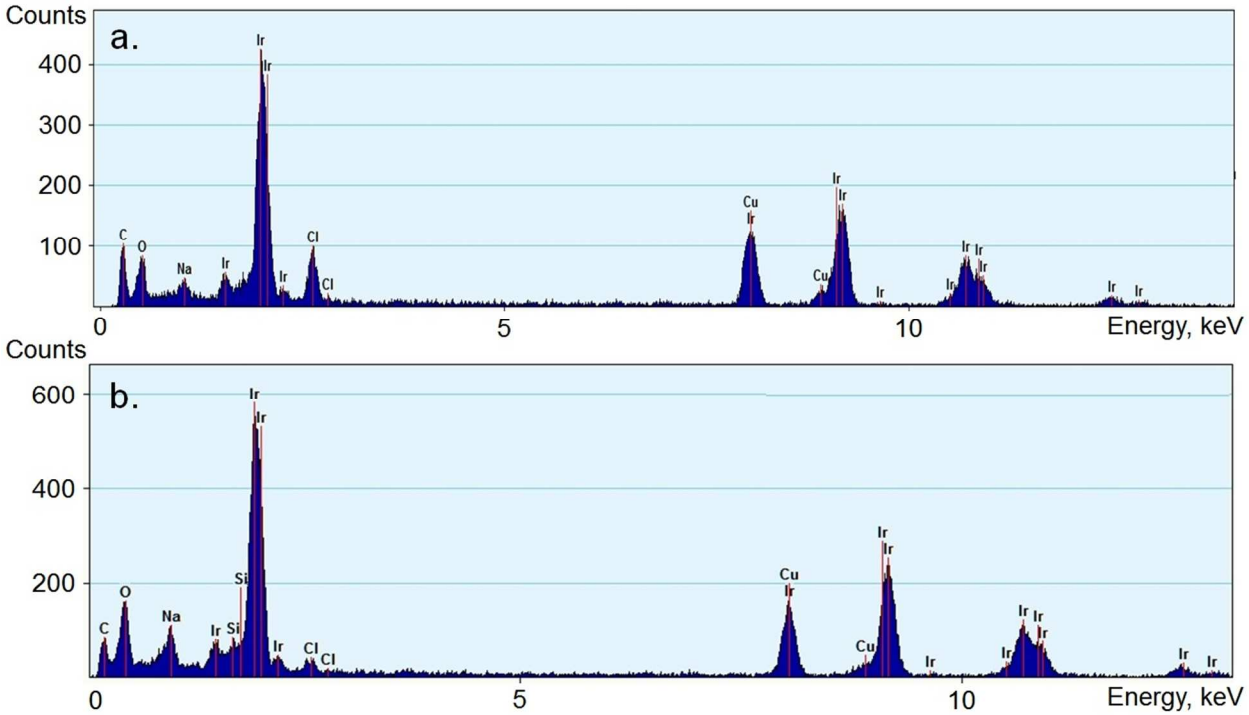

Figure S1. EDX spectra of IrO_2 prepared by Adams Fusion method starting from $IrCl_3 \cdot xH_2O$ (Strem Chemicals) for 30'@350°C (a) and 5h@500°C (b).

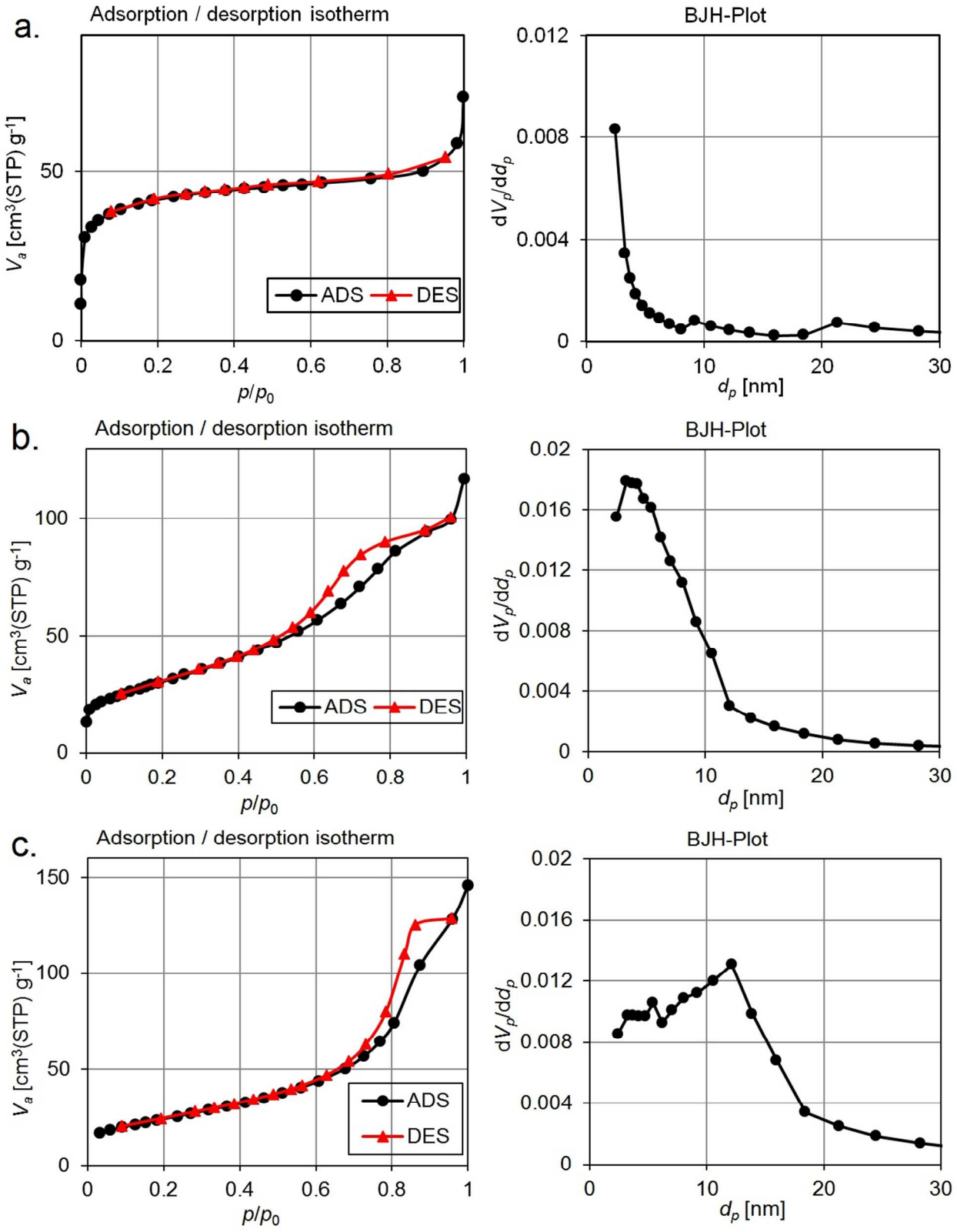
a.
Adsorption / desorption isotherm
V_a [cm³(STP) g⁻¹]
p/p_0
ADS
DES
BJH-Plot
dV_p/dd_p
d_p [nm]
b.
Adsorption / desorption isotherm
V_a [cm³(STP) g⁻¹]
p/p_0
ADS
DES
BJH-Plot
dV_p/dd_p
d_p [nm]
c.
Adsorption / desorption isotherm
V_a [cm³(STP) g⁻¹]
p/p_0
ADS
DES
BJH-Plot
dV_p/dd_p
d_p [nm]

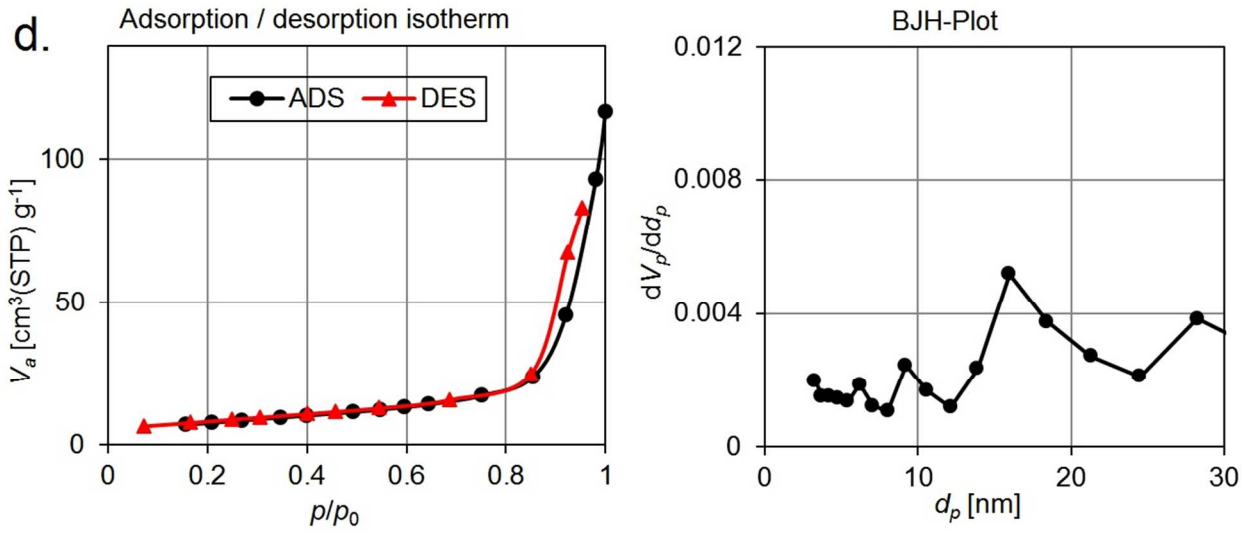

Figure S2. N_2 adsorption/desorption isotherms and BJH plots for IrO_2−150 (a), IrO_2−110 (b), IrO_2−90 (c), IrO_2−30 (d).

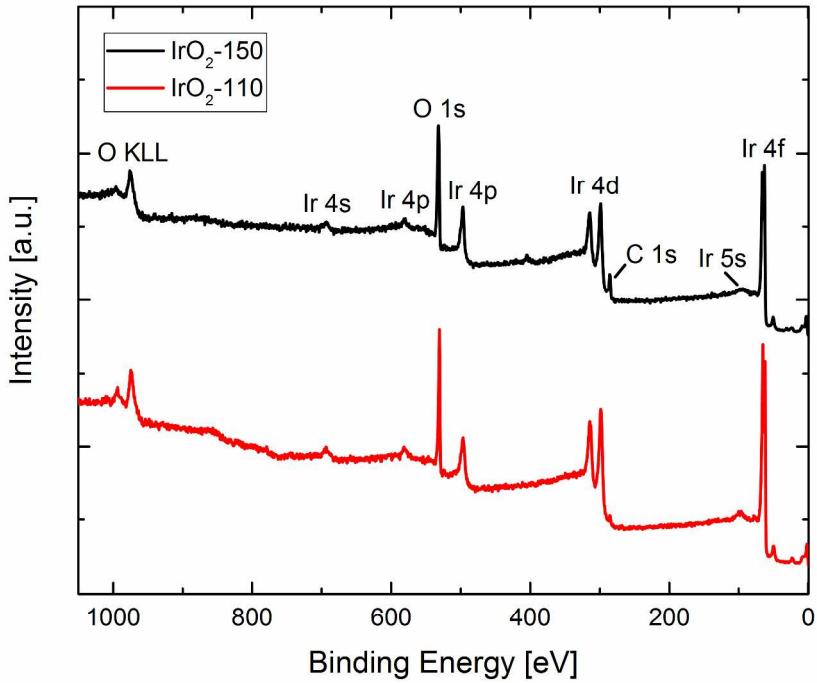

Figure S3. XPS survey scans of IrO_2−150 and IrO_2−30.

EXAFS Analysis

Extended X−ray absorption fine structure (EXAFS) data were analyzed using the Demeter program package, which included energy calibration (based on the simultaneously measured Pt reference foil), background subtraction, and edge step normalization. The resulting spectra were converted to the photoelectron wave vector *k* (in units $Å^{-1}$) by assigning the

photoelectron energy origin, E_0, corresponding to k = 0, to the first inflection point. The resulting χ(k) functions were weighted with k^2 to compensate for the dampening of the XAFS amplitude with increasing k. These χ(k) functions were Fourier transformed over 3–17 $Å^{-1}$ for the dry catalyst samples. The amplitude reduction factor, S_0^2, was calculated using FEFF code from the Ir scattering paths of sample IrO_2–30 assuming the coordination numbers based on the IrO_2 rutile crystal structure. This is a reasonable assumption given that IrO_2–30 most closely represents bulk IrO_2 as evidenced by the high degree of crystallinity observed in XRD (Figure 2) and the large particle size seen in the TEM analysis (Figure 1f). The determined value of S_0^2 = 0.76 was then used in all subsequent FEFF calculations for IrO_2–30 and IrO_2–150 while the coordination number, bond distance, and Debye-Waller factor parameters were allowed to vary.

In order to directly compare IrO_2–30 and IrO_2–150, a simple two–shell model based on the rutile crystal structure was employed to fit the EXAFS data. A single Ir–O scattering path was used to describe the 6 nearest neighbor oxygen atoms (R_{eff} = 1.999 Å) in the first coordination shell. Two additional Ir–Ir scattering paths (R_{eff} = 3.159 and 3.556 Å) were used in fitting the second shell for IrO_2–30. The inclusion of any further scattering paths did not improve the quality of the fit significantly. Only one of the Ir–Ir scattering paths (R_{eff} = 3.159 Å) was used in the best fit of IrO_2–150. This was sufficient to achieve a reasonable fit that encompassed the majority of the scattering signal, as can be seen by the best fit of χ(Re) (Figure 4d) and the photoelectron wave vector, χk^2 (Figure S4). The best fit of the first Ir–O shell for both samples remained relatively unchanged with the inclusion of the Ir–Ir scattering path(s).

The same EXAFS fitting approach used for the dry catalyst samples was also used for the *operando* EXAFS data. In this case, however, the χ(k) functions were Fourier transformed over 3–14 $Å^{-1}$ for sample IrO_2–30 and 3–10 $Å^{-1}$ for IrO_2–150 due to the noise encountered at higher potentials or, in the case of the stability measurements, after many potential cycles.

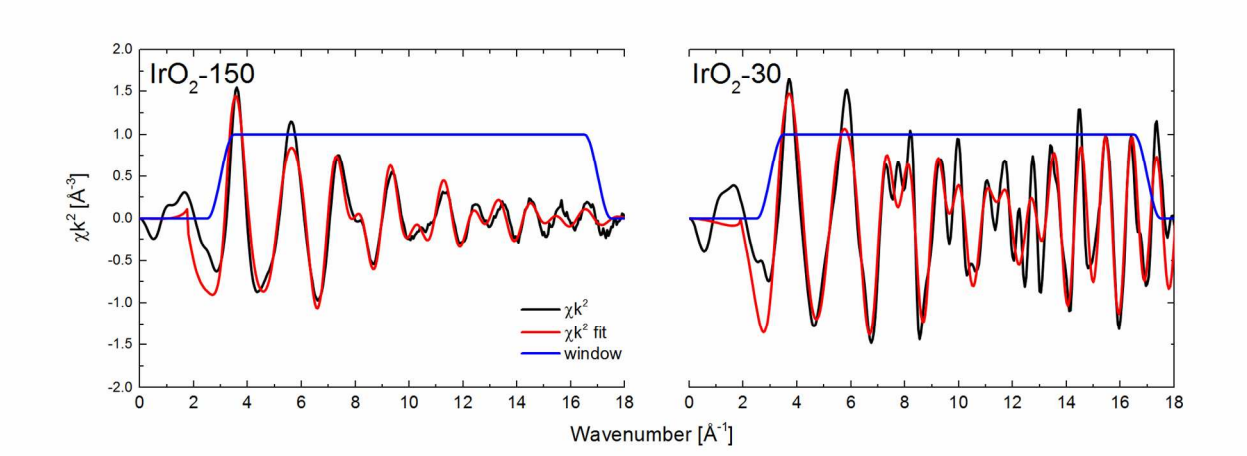

Figure S4. EXAFS fits for the IrO_2–150 and IrO_2–30 dry catalyst samples in k-space.

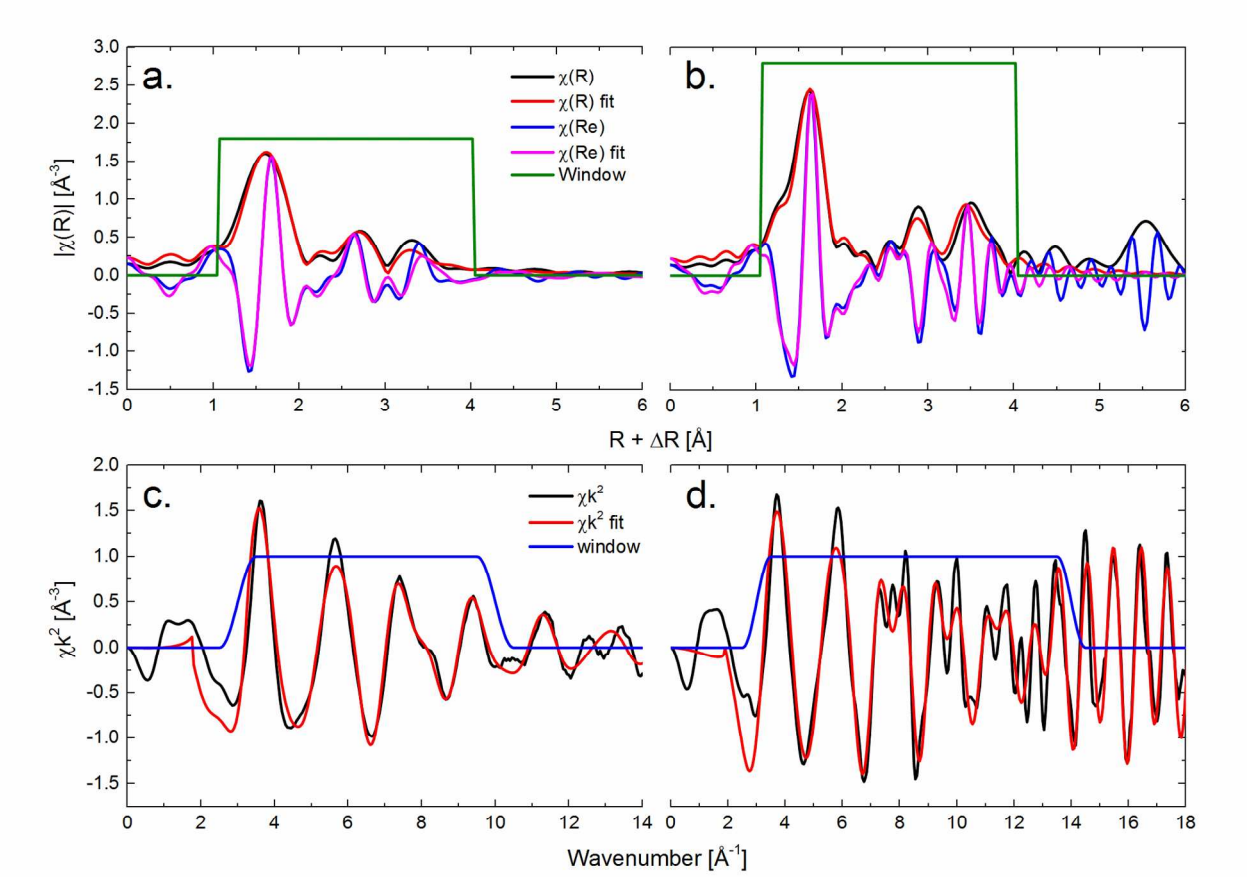

Figure S5. Typical examples of the fitted Fourier transformed Ir EXAFS spectra measured at 1.00 V (anodic scan) during the *operando* OER polarization for IrO_2−150 (a) and IrO_2−30 (b) in R-space and for IrO_2−150 (c) and IrO_2−30 in (d) in *k*-space.

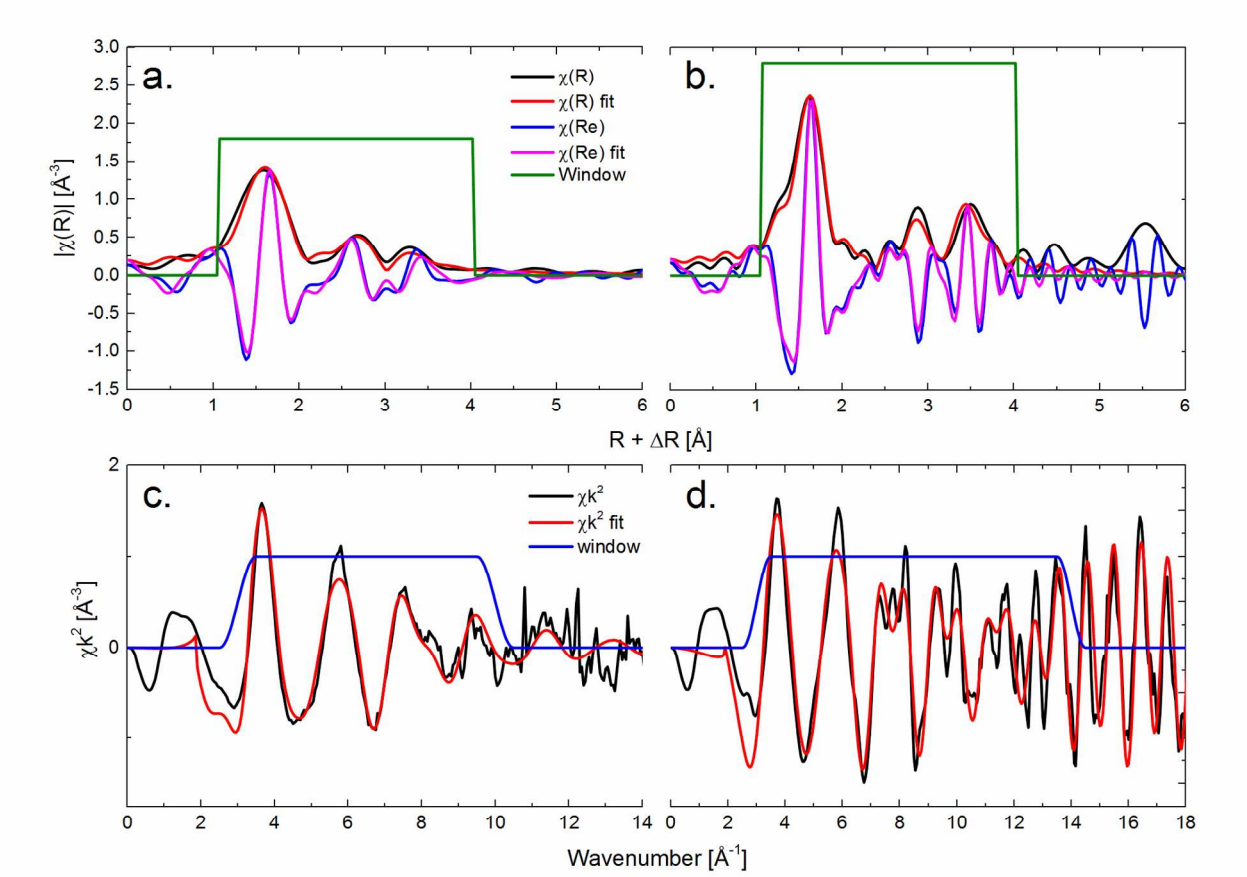

Figure S6. Typical examples of the fitted Fourier transformed Ir EXAFS spectra measured at 1.50 V (anodic scan) during the *operando* OER polarization for IrO_2−150 (a) and IrO_2−30 (b) in R-space and for IrO_2−150 (c) and IrO_2−30 in (d) in *k*-space.

Table S1. Summary of the EXAFS best fit parameters for the prepared IrO_2 samples recorded at different electrode potentials. *Operando* X−ray absorption spectra were measured at the Ir−L_{III} edge during a standard electrochemical OER polarization measurement. *N* denotes the coordination number of the given scattering path, *d* indicates the refined path length, σ^2 represents the Debye-Waller factor, ΔE_0 is the energy shift, and the R-factor represents the relative error of the fit and data. An amplitude reduction factor of $S_0^2 = 0.76$ was used for all fits. *k* was kept within the range of *k* = 3-14 Å^{-1} for sample IrO_2−30 and *k* = 3−10 Å^{-1} for IrO_2−150. A fitting window of 4 Å in R-space was used in all cases. The subscripts A and C indicate the anodic and cathodic polarization, respectively, with regards to the applied potential.

Potential, V	*Scattering Path*	*N*	*d, Å*	*σ^2, Å^2*	*ΔE_0, eV*	*R-factor*
IrO_2−150						
1.00_A	Ir−O	5.4 ± 0.8	2.020 ± 0.011	0.0024 ± 0.0021	12.9 ± 1.1	0.029
	Ir−Ir1	15.3 ± 7.4	3.126 ± 0.027	0.0164 ± 0.0064		
1.10	Ir−O	6.6 ± 1.0	2.014 ± 0.012	0.0043 ± 0.0022	11.9 ± 1.2	0.028
	Ir−Ir1	14.1 ± 7.5	3.115 ± 0.027	0.0152 ± 0.0065		
1.20	Ir−O	6.7 ± 1.1	2.010 ± 0.013	0.0049 ± 0.0025	11.8 ± 1.3	0.031
	Ir−Ir1	13.4 ± 7.5	3.110 ± 0.029	0.0148 ± 0.0070		
1.30	Ir−O	5.3 ± 0.8	2.012 ± 0.011	0.0030 ± 0.0020	13.4 ± 1.1	0.027
	Ir−Ir1	15.1 ± 6.8	3.123 ± 0.026	0.0166 ± 0.0060		
1.40	Ir−O	5.2 ± 0.8	2.008 ± 0.011	0.0030 ± 0.0020	13.0 ± 1.2	0.028
	Ir−Ir1	14.5 ± 6.9	3.123 ± 0.026	0.0178 ± 0.0074		
1.44	Ir−O	6.6 ± 1.1	2.008 ± 0.014	0.0070 ± 0.0028	13.0 ± 1.2	0.031
	Ir−Ir1	11.3 ± 5.8	3.116 ± 0.026	0.0128 ± 0.0059		
1.50	Ir−O	5.6 ± 1.0	2.006 ± 0.014	0.0050 ± 0.0026	13.3 ± 1.2	0.035
	Ir−Ir1	14.8 ± 7.7	3.110 ± 0.032	0.0181 ± 0.0077		
1.00_C	Ir−O	5.4 ± 0.8	2.023 ± 0.011	0.0027 ± 0.0021	13.1 ± 1.1	0.028
	Ir−Ir1	14.4 ± 0.8	3.133 ± 0.028	0.0163 ± 0.0066		
IrO_2−30						
1.00_A	Ir−O	6.0 ± 0.6	1.991 ± 0.007	0.0017 ± 0.0010	13.2 ± 1.0	0.035
	Ir−Ir1	5.1 ± 2.4	3.151 ± 0.007	0.0049 ± 0.0025		
	Ir−Ir2	3.7 ± 1.9	3.548 ± 0.007	0.0008 ± 0.0019		
1.20	Ir−O	6.0 ± 0.6	1.991 ± 0.008	0.0017 ± 0.0011	13.4 ± 1.0	0.036
	Ir−Ir1	5.4 ± 2.5	3.151 ± 0.008	0.0051 ± 0.0026		
	Ir−Ir2	3.5 ± 1.9	3.548 ± 0.008	0.0005 ± 0.0020		
1.30	Ir−O	5.8 ± 0.6	1.992 ± 0.008	0.0016 ± 0.0011	13.5 ± 1.0	0.035
	Ir−Ir1	5.4 ± 2.5	3.152 ± 0.008	0.0053 ± 0.0027		
	Ir−Ir2	3.2 ± 1.8	3.549 ± 0.008	0.0002 ± 0.0020		
1.40	Ir−O	5.9 ± 0.6	1.990 ± 0.008	0.0016 ± 0.0011	13.3 ± 1.0	0.039
	Ir−Ir1	5.9 ± 2.8	3.150 ± 0.008	0.0060 ± 0.0029		
	Ir−Ir2	3.7 ± 2.1	3.547 ± 0.008	0.0010 ± 0.0021		
1.44	Ir−O	6.0 ± 0.6	1.989 ± 0.008	0.0022 ± 0.0012	13.2 ± 1.1	0.043
	Ir−Ir1	4.8 ± 2.5	3.149 ± 0.007	0.0046 ± 0.0028		
	Ir−Ir2	3.2 ± 1.9	3.546 ± 0.007	0.0002 ± 0.0021		
1.50	Ir−O	5.9 ± 0.6	1.989 ± 0.008	0.0018 ± 0.0011	13.3 ± 1.0	0.036
	Ir−Ir1	5.2 ± 2.6	3.149 ± 0.008	0.0053 ± 0.0028		
	Ir−Ir2	3.3 ± 1.9	3.546 ± 0.008	0.0003 ± 0.0020		
1.00_C	Ir−O	6.0 ± 0.6	1.988 ± 0.008	0.0019 ± 0.0011	13.0 ± 1.0	0.036
	Ir−Ir1	5.8 ± 2.7	3.148 ± 0.008	0.0060 ± 0.0030		
	Ir−Ir2	3.7 ± 2.1	3.545 ± 0.008	0.0010 ± 0.0021		

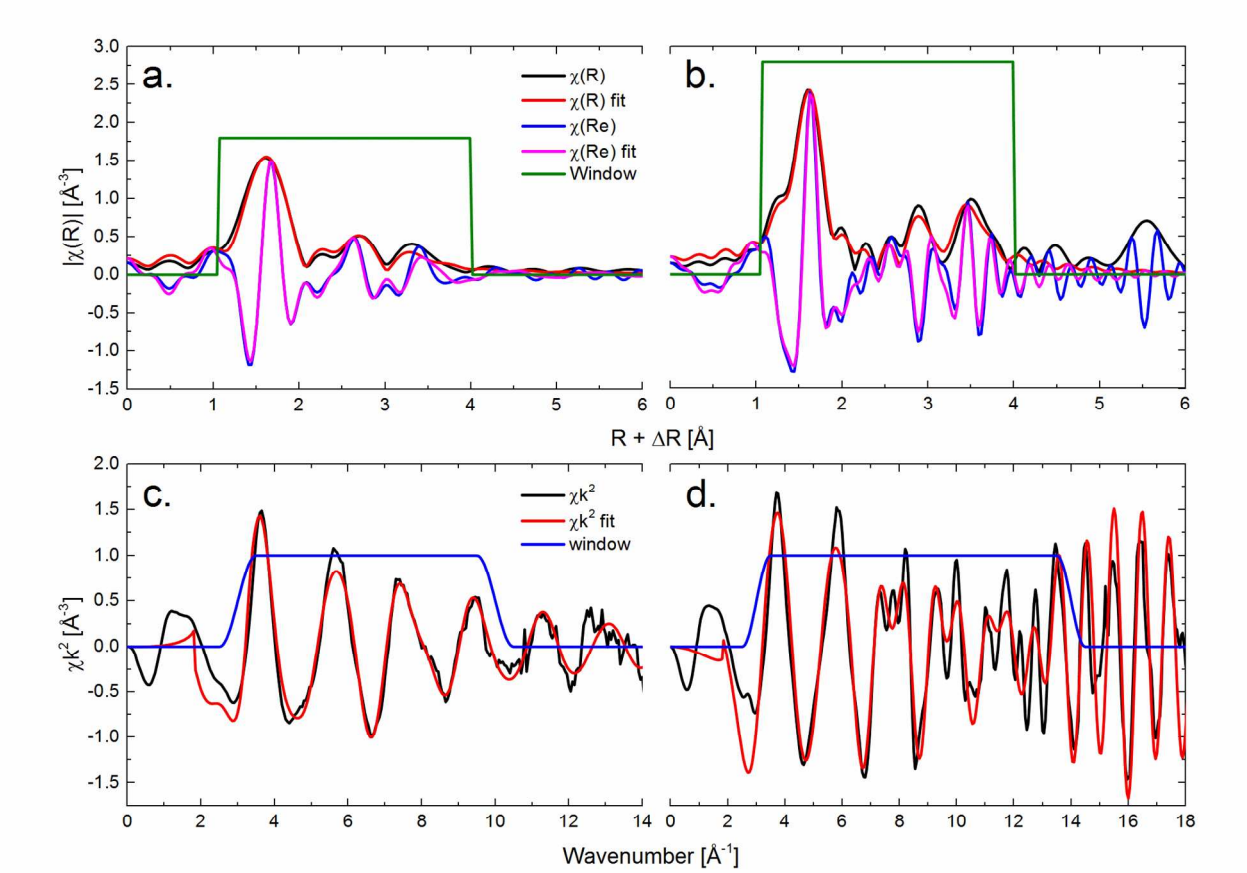

Figure S7. Typical examples of the fitted Fourier transformed Ir EXAFS spectra recorded during the *in situ* stability measurements (shown at the initial state, i.e. after 0 cycles; recorded at 1.00 V) for IrO_2−150 (a) and IrO_2−30 (b) in R-space and for IrO_2−150 (c) and IrO_2−30 (d) in *k*-space.

Table S2. Summary of the EXAFS best fit parameters for the prepared IrO_2 samples recorded during the *in situ* stability measurements at the Ir−L_{III} edge after 0, 100 and 250 cycles. *N* denotes coordination number of the given scattering path, *d* indicates the refined path length, σ^2 represents the Debye-Waller factor, ΔE_0 is the energy shift, and the R-factor represents the relative error of the fit and data. An amplitude reduction factor of $S_0^2 = 0.76$ was used for all fits. *k* was kept within the range of *k* = 3-14 Å^{-1} for sample IrO_2−30 and *k* = 3−10 Å^{-1} for IrO_2−150. A fitting window of 4 Å in R-space was used in all cases.

Cycle #	*Scattering Path*	*N*	*d, Å*	*σ^2, Å^2*	*ΔE_0, eV*	*R-factor*
IrO_2−150						
0	Ir−O	4.7 ± 0.6	2.018 ± 0.010	0.0011 ± 0.0018	13.0 ± 1.0	0.022
	Ir−Ir1	16.8 ± 7.4	3.121 ± 0.027	0.0194 ± 0.0068		
100	Ir−O	5.0 ± 0.7	2.020 ± 0.011	0.0016 ± 0.0021	13.5 ± 1.1	0.028
	Ir−Ir1	14.1 ± 6.6	3.127 ± 0.027	0.0156 ± 0.0064		
250	Ir−O	5.5 ± 0.8	2.030 ± 0.012	0.0035 ± 0.0022	14.1 ± 1.1	0.032
	Ir−Ir1	13.7 ± 6.8	3.139 ± 0.028	0.0160 ± 0.0066		
IrO_2−30						
0	Ir−O	6.1 ± 0.6	1.983 ± 0.008	0.0020 ± 0.0012	12.6 ± 1.2	0.045
	Ir−Ir1	3.3 ± 2.0	3.143 ± 0.008	0.0025 ± 0.0026		
	Ir−Ir2	3.7 ± 2.0	3.540 ± 0.008	0.0004 ± 0.0019		
100	Ir−O	6.0 ± 0.6	1.998 ± 0.009	0.0025 ± 0.0013	14.1 ± 1.1	0.053
	Ir−Ir1	6.7 ± 3.1	3.158 ± 0.009	0.0065 ± 0.0030		
	Ir−Ir2	3.6 ± 2.2	3.555 ± 0.009	0.0010 ± 0.0023		
250	Ir−O	5.9 ± 0.6	1.991 ± 0.008	0.0017 ± 0.0011	14.0 ± 1.0	0.035
	Ir−Ir1	5.6 ± 2.6	3.151 ± 0.008	0.0059 ± 0.0028		
	Ir−Ir2	3.4 ± 1.9	3.548 ± 0.008	0.0008 ± 0.0022		